ACS SENSORS

pubs.acs.org/acssensors Article

Tracking the Dynamic Histone Methylation of H3K27 in Live Cancer Cells

Ya Gong, Chujun Wei, Leonardo Cheng, Fengyi Ma, Shaoying Lu, Qin Peng, Longwei Liu,* and Yingxiao Wang*

Cite This: *ACS Sens.* 2021, 6, 4369–4378 Read Online

ACCESS | Metrics & More | Article Recommendations | Supporting Information

ABSTRACT: Histone methylations play a crucial role in chromatin remodeling and genome regulations. However, there is a lack of tools to visualize these histone modifications with high spatiotemporal resolutions in live cells. We have developed a biosensor based on fluorescence resonance energy transfer (FRET) and incorporated it into nucleosomes, capable of monitoring the trimethylation of H3K27 (H3K27me3) in live cells. We also revealed that the performance of the FRET biosensor can be significantly improved by adjusting the linkers within the biosensor. An improved biosensor enables the live-cell imaging of different histone methylation status, induced by the suppressive H3.3K27M or existing in breast cancer cells with varying genetic backgrounds. We have further applied the biosensor to reveal the dynamic coupling between H3K27me3 changes and caspase activity representing the initiation of apoptosis in cancer cells by imaging both H3K27me3 and caspase activity simultaneously in the same live cells. Thus, this new FRET biosensor can provide a powerful tool to visualize the epigenetic regulation in live cells with high spatial temporal resolutions.

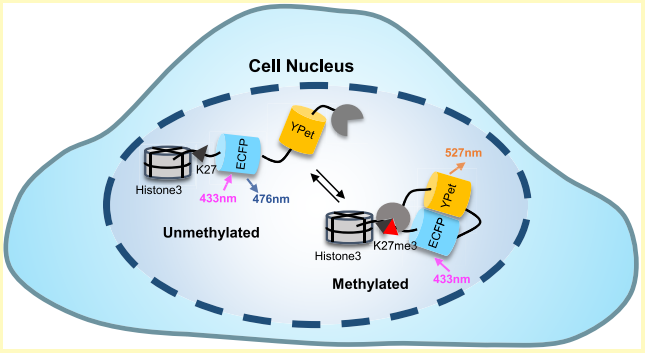

KEYWORDS: *FRET, histone modification, H3K27me3, apoptosis, live-cell imaging*

Histone proteins in chromatin can undergo various modifications, including methylation, acetylation, phosphorylation, ubiquitylation, and sumoylation.[1] Of these histone modifications, histone methylation is a vital epigenetic regulation that mainly occurs on the side chain of lysine and arginine, in which lysine can be mono-, di-, or trimethylated, whereas arginine can only be mono- and dimethylated due to their respective chemical characteristics.[2] Indeed, histone methylations have a profound impact on cellular processes, including cell cycle control, senescence, cell fate decisions, and tumorigenesis.[3] Specifically, histone 3 lysine 27 trimethylation (H3K27me3), catalyzed mainly by the enhancer of the zeste homolog (EZH2), is associated with transcriptional silencing and heterochromatin formation.[4−6]

The dysregulation of H3K27me3 and its modifiers is frequently found in various cancers, including but not limited to prostate cancer,[7] endometrial carcinoma,[8] pediatric glioma,[9] and breast cancers.[10] For instance, the histone H3.3K27M mutation, which has been demonstrated to sufficiently reduce the amounts of endogenous H3K27me3 *in vitro*,[11] was found in 60% of high-grade pediatric glioma cases with a median survival of about one year in patients after diagnosis.[9] Furthermore, different types of cancer with various genetic backgrounds have diverse epigenetic levels, leading to the differential epigenetic adaptation and responses of cancer cells to chemotherapy. For example, MDA-MB-231, a poorly differentiated triple-negative breast cancer cell line that lacks estrogen receptors (ER), progesterone receptor expression, and human epidermal growth receptor 2 (HER2),[12] is less sensitive to the widely used drug tamoxifen, a selective estrogen receptor modulator,[13] than the ER-positive MCF-7 cell.[13] Consistently, it was reported that MDA-MB-231 cells have a higher expression of the EZH2 and H3K27me3 than MCF-7 cells,[14] which may have contributed to the drug resistance of MDA-MB-231 cells. Since the H3K27me3 level at genomic loci has also been well-established to affect gene repressions, it has become a popular target for epigenetic research and anticancer drug development.[15,16] However, there is a lack of tools to monitor and track H3K27me3 in live cells, which hinders the related studies.

The induction of apoptosis in target cancer cells is a common therapeutic strategy in cancer therapy.[17] At the same time, the increase in antiapoptosis capacity is commonly

Received: August 5, 2021
Accepted: November 29, 2021
Published: December 8, 2021

observed in most of the chemotherapy-resistant cancers,[18,19] resulting in tumor survival, drug resistance, or recurrence of cancer. Epigenetic modifications have been reported to be closely correlated with drug resistance and response in cancer cells, but the underlying mechanism still remains unclear.[20−22] The H3K27me3 writer EZH2 has been demonstrated to be frequently overexpressed in a wide variety of human cancers[23] and directly regulates cancer cell death.[24] A previous study has shown that the inhibition of the EZH2 in osteosarcoma cells led to cisplatin resistance by decreasing the H3K27me3 levels.[25] In other cases, triptolide, an antitumor drug candidate, could trigger caspase-dependent apoptosis of myeloma cells by decreasing the trimethylation of histone H3K27.[26,27] However, despite these reported interplays between epigenetic modifications and drug response in cancer cells, the kinetics of histone modifications, such as H3K27me3, in drug-induced apoptotic cells is still unclear, especially in a single live cell. The revelation of this interactive information on the epigenetic modifications and the apoptotic process would lead to a deeper understanding of epigenetic modifications under chemotherapy and facilitate the development of anticancer drugs and better therapeutic strategies.

Most of the current studies on the association between histone methylation and cell phenotypes are based on genome-wide or locus-specific chromatin immunoprecipitation followed by sequencing (ChIP-seq) studies.[28] However, since chromatin is extracted from cells during the ChIP-seq process, it is difficult to visualize and quantify the spatiotemporal characteristics of H3K27me3 under its natural context inside a single living cell. Genetically encoded biosensors based on fluorescence resonance energy transfer (FRET) can provide a powerful tool in visualizing the dynamics of epigenetic modifications at subcellular levels. For instance, recombinant protein probes with the epigenetic modification recognition domain of H3K14ac[29] or heterochromatin[30] were developed to directly monitor the spatial distribution and abundance in the cell nucleus. In addition, modular bimolecular fluorescence complementation (BiFC)-based sensors were also developed to detect the DNA methylation and H3K9me3 at endogenous genomic sites in live cells.[31] In addition, intramolecular FRET biosensors have the advantages of a high signal-to-noise ratio and simple radiometric image analysis.[32−34] These FRET biosensors have been successfully used to visualize the activities of cellular signaling molecules such as Ca^{2+}, phospholipids, and protein kinases.[35,36] For the imaging of epigenetic modifications, the FRET-based biosensor of histone H4 hyperacetylation enables the real-time monitoring of dynamic fluctuations of histone H4 acetylation[37] or H4K12-specific acetylation[38] levels during cell mitosis and in response to inhibitors. However, since the development of FRET biosensors often requires tedious and substantial trial-and-error experiments, few biosensors have been developed to visualize the H3K27me3 changes in live cells. Previously, a histone methylation reporter based on a partial H3 peptide and a methyllysine binding domain was developed,[39] which could be used to detect methyltransferase or demethylase activity to represent the averaged methylation level in the nucleus. However, this reporter was not integrated into the nucleosomes and hence may have difficulty in monitoring the *in situ* histone methylation occurring at the nucleosomes. Furthermore, this reporter was not tested in live cells over prolonged periods for tracking biological processes in cancer cells under drug treatment and showed a relatively mild contrast between the methylated and nonmethylated states.

In this study, we have constructed an H3K27me3 FRET biosensor with relatively high specificity and a large dynamic range in live cells. Different from the previous design of the H3K27me3 biosensor, in which the biosensors diffuse in the whole nucleus,[39] our biosensor adopted a different structure and utilized the entire H3 protein so that the biosensor can be integrated into nucleosomes to report and quantify the histone changes *in situ*, which led to an enhanced FRET contrast. We further improved the sensitivity of this FRET biosensor by adjusting the linker length, which may provide a general strategy to enhance the sensitivity for other epigenetic FRET biosensors. Our H3K27me3 FRET biosensor, together with a caspase biosensor, further allowed the simultaneous visualization of H3K27me3 changes and caspase activity to reveal their spatiotemporal interplays in single live cancer cells.

RESULTS

Engineering the Prototype H3K27me3 Biosensor. Our prototype biosensors were assembled based on the previous methylation reporters[39] and an H3K9me3 reporter from our group.[25] Specifically, a truncated *Drosophila* polycomb (Pc) chromodomain (residues 21 to 78) was used as the binding domain to H3K27me3 of the histone. Additionally, ECFP/YPet, the optimized FRET pair, was linked together with an EV linker (primary linker) and sandwiched between the binding domain and histone H3 as the substrate. Since the biosensor is connected to the full-length H3, it can be directly integrated into nucleosomes to quantify the histone changes. We hypothesized that when H3K27 is not trimethylated, the biosensor stays at its "off" state, with the fluorescent proteins relatively far away from each other containing little FRET; when H3K27 is trimethylated, the Pc domain binds to H3K27me3, which converts the biosensor into an "on" state, bringing YPet closer to ECFP to cause a stronger FRET. As such, by calculating the ratio of FRET/ECFP in single live cells, we can visualize and track the trimethylation dynamics on H3K27 (Figure 1a).

The wild type and its corresponding mutant biosensors were able to precisely locate into the cell nucleus without any significant effects on the viability of the cells (Figure 1b,c). In order to validate that FRET only occurs when H3K27 is trimethylated, we created two biosensor mutants, the 27 lysine-to-leucine (K27L) or lysine-to-methionine (K27M) mutation to eliminate the H3K27 methylation substrate in the biosensor, and compared their signals to that of the wild-type biosensor.[40] When the FRET ratio of different experimental groups was measured, the wild-type (WT) biosensor had a higher FRET ratio than the K27L or K27M biosensor (Figure 1b), indicating the specificity of the biosensor FRET signal in detecting H3K27me3 levels in live cells. H3K27M has been previously reported to inhibit global endogenous H3K27me3 by sequestrating the H3K27 methyltransferase EZH2.[11] Consistently, we observed lower FRET signals from the K27M biosensor group (Figure 1b). The change of the average FRET/ECFP ratio of the prototype biosensor upon mutation is around 13% (WT vs K27M), suggesting a moderate sensitivity of the biosensor.

Optimization of Linkers Improves the H3K27me3 FRET Biosensor. To investigate whether a flexible linker in between the Pc domain and YPet (linker-1) could further improve the sensitivity of the biosensor, we inserted an

https://doi.org/10.1021/acssensors.1c01670
ACS Sens. 2021, 6, 4369−4378

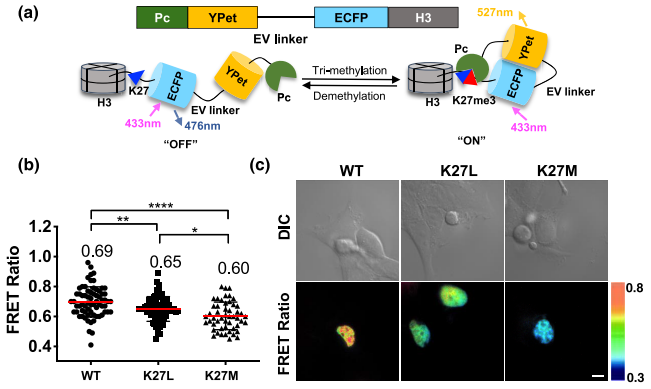

Figure 1. Construction and characterization of the prototype H3K27me3 biosensor. (a) Schematic drawing of the domain structures and the proposed activation mechanism of the prototype H3K27me3 biosensor. (b) Basal FRET ratios of the wild-type and mutant prototype biosensors (K27L and K27M) inside the HEK cells. From left to right, n = 69, 71, and 51, with $^{**}p$ = 0.0079, $^{*}p$ = 0.0182, and $^{****}p < 0.0001$, one-way ANOVA. Error bars, mean ± SD. (c) Representative DIC and FRET ratio images of the wild-type and mutant prototype biosensors (K27L and K27M) expressed inside HEK cells (scale bar, 10 μm).

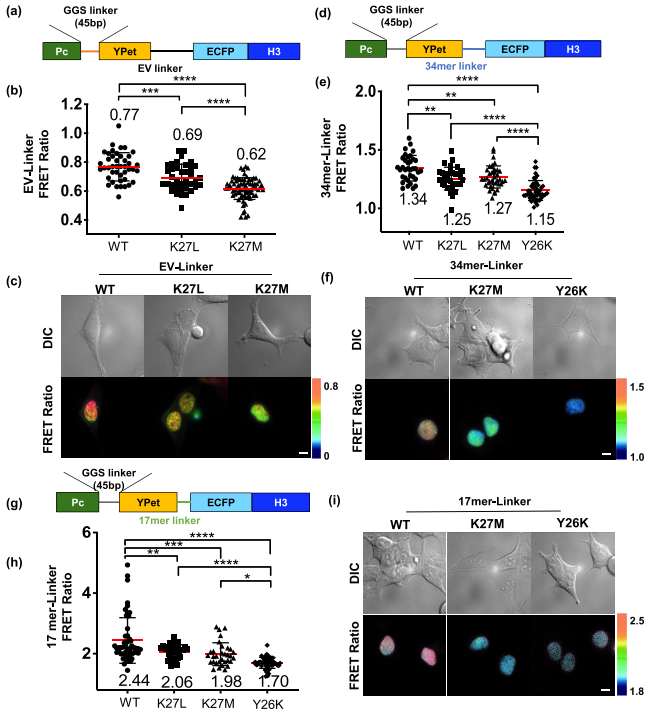

Figure 2. Varying linker length improves the sensitivity of the biosensor. (a) Schematic drawing of the biosensor with a primary EV linker and an additional 15-mer GGS linker in between the Pc domain and YPet. (b,c) Quantified FRET ratio averages of the wild-type and mutant (K27L and K27M) biosensors with a primary EV linker and an additional 15-mer GGS linker (b) and their representative DIC and FRET ratio images (c) in HEK cells. One-way ANOVA, from left to right, n = 43, 37, and 73, with $^{***}p$ = 0.0005 and $^{****}p < 0.0001$. (d) Schematic drawing of the GGS-linker biosensor with a primary 34-mer linker. (e,f) Quantified FRET ratio averages of the wild-type and mutant (K27L, K27M, and Y26K) GGS-linker biosensors with a primary 34-mer linker (e) and their DIC and FRET ratio images (f) in HEK cells. From left to right, n = 35, 32, 38, and 47, with $^{**}p$ = 0.0013 and 0.0059 and $^{****}p < 0.0001$, one-way ANOVA. (g) Schematic drawing of the GGS-linker biosensor with a primary 17-mer linker. (h,i) Quantified FRET ratio averages of the wild-type and mutant (K27L, K27M, and Y26K) GGS-linker biosensors with a primary 17-mer linker (h) and their DIC and FRET ratio images (i) in HEK. From left to right, n = 52, 36, 32, and 50, with $^{**}p$ = 0.0015 and 0.0037, $^{***}p$ = 0.0002, $^{****}p < 0.0001$, and $^{*}p$ = 0.0408, one-way ANOVA.

additional GGS linker of 15 amino acids (aa) in the prototype biosensor in between the Pc domain and YPet (Figure 2a). While retaining its specificity, the FRET efficiency of the GGS-linker biosensor was significantly improved compared to the prototype biosensor (Figure 2b,c). The ratios of both the prototype and the GGS-linker biosensors without their H3K27 trimethylation were similar, as shown by the results of their K27M mutants (Figures 1b and 2b). This suggests that the 15-mer GGS linker, while without affecting the FRET levels when the FRET pair of a donor and an acceptor is sufficiently separated, could have provided a better binding orientation of the FRET pair in the presence of H3K27me3 for a stronger FRET signal. It is also worth noticing that the relative positions of the binding domain and the substrate in the biosensor play a critical role in FRET sensitivity. This was illustrated by swapping the locations of the YPet and Pc domains in the biosensor. Either with or without a GGS linker, the change in the relative position between Pc and H3 has led to dysfunctional biosensors (Figure S1). Nevertheless, after this additional 15-mer GGS-linker insertion, the FRET ratio contrast between the "on" and "off" states of the biosensor increased to 24.2%.

The FRET efficiency of intramolecular FRET biosensors is dependent primarily on the distance and relative orientation of the two fluorophores,[35] which can be controlled by the linker between the FRET donor and acceptor (primary linker). Thus, we hypothesized that decreasing the linker length between YPet and ECFP would increase the FRET efficiency of the biosensor in live cells since the binding affinity from the Pc domain to H3K27me3 is moderate (K_d = 5 μM).[41] Decreasing the linker length may hence increase the probability of interaction between the binding domain and the H3 substrate when trimethylated.

To test this hypothesis, we replaced the primary EV linker (120-mer) with a 34-mer linker[42] and a 17-mer linker[43] on the GGS-linker biosensors. Indeed, with the decrease in the linker length, the basal FRET ratio increased significantly as the distance between the donor and the receptor decreased (Figure 2d–i). These biosensor variants with different linkers also maintained their specificity and nuclear localization (Figure 2f,i). The FRET signal was further confirmed to be mediated by the methylation of the H3K27 tail and the binding of the Pc domain, as we designed. Indeed, when a point mutation on the binding domain (Y26K[41]) was introduced, the biosensor FRET ratio decreased significantly (Figure 2e,h). Overall, among the different primary linkers, the 17-mer linker biosensor (GGS17-H3K27me3 biosensor) showed the best performance as the FRET contrast between its "on" and "off" states increased to 43.5% (Figure 2g–i). It should be noted that the 15-mer GGS linker and the primary linker play synergistic roles in determining the biosensor performance because changing only the primary linker did not lead to such a significant improvement of the biosensor (Figure S2). Furthermore, with this optimized GGS17-H3K27me3 biosensor, a strong correlation of the FRET ratio signal of the wild-type FRET biosensor with the immunofluorescence image of H3K27me3 was observed in the nucleus. In contrast, the

https://doi.org/10.1021/acssensors.1c01670
ACS Sens. 2021, 6, 4369–4378

control biosensor with a Y26K mutation did not show a clear pattern and correlation to the immunofluorescence data (Figure S3). These results suggest a high fidelity of our nucleosome-incorporated biosensor in reporting the spatial distribution of H3K27me3 epigenetics.

In summary, by optimizing the linkers in the prototype biosensor, we have successfully generated a FRET biosensor with improved sensitivity that is capable of monitoring H3K27me3 levels in the live-cell nucleus. We named this biosensor GGS17-H3K27me3, which is used in the remaining text.

The GGS17-H3K27me3 Biosensor Is Capable of Detecting the H3.3K27M-Induced Epigenetic Changes. The histone H3.3K27M mutation, which was found in 60% of high-grade pediatric glioma cases,[9] has been demonstrated to sufficiently reduce the level of endogenous H3K27me3 *in vitro*.[11] To validate that the GGS17-H3K27me3 biosensor can be applied in quantifying the H3.3K27M-induced epigenetic changes, specifically H3K27me3, we generated HEK cell lines stably expressing the FLAG-H3.3K27M mutant (H3.3M) or wild-type H3.3 (H3.3WT). Western blotting revealed that the H3.3K27M cell line has minimal H3K27me3 in both the exogenous biosensors and endogenous H3 proteins, compared to the cells that express WT-H3.3 (Figure 3a). The GGS17-H3K27me3 biosensor also showed a significantly higher FRET ratio in the H3.3WT cell line than in the H3.3K27M cell line, accurately reflecting the suppressed H3K27me3 levels caused by the expression of H3.3K27M (Figure 3b,c).

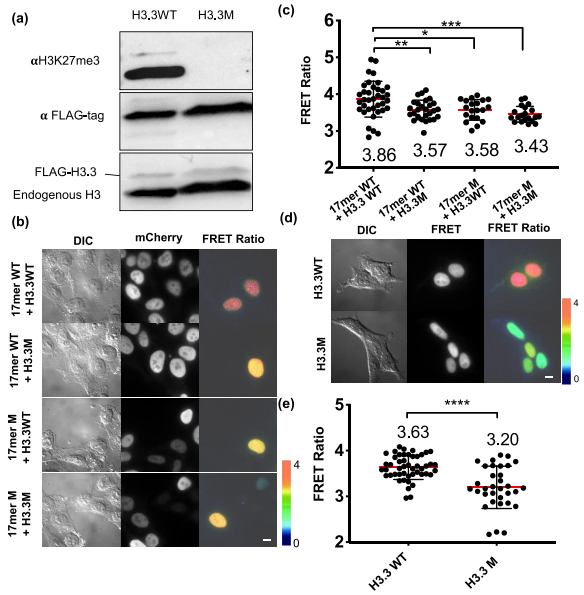

Figure 3. Detecting the H3.3M mutation-induced suppression of H3K27me3 signals. (a) Immunoblots of trimethylation levels on endogenous H3 and FLAG-H3.3 in H3.3WT and H3.3M HEK cell lines. (b) Representative images of the biosensor (FRET ratio) and FLAG-H3.3 (mCherry) in fixed H3.3WT and H3.3M cells. (c) Basal FRET ratios of the wild-type and mutant (K27M) GGS17-H3K27me3 biosensors in H3.3WT and H3.3M HEK cells lines (left). From left to right, n = 38, 27, 20, and 22, with $^{**}p$ = 0.0087, $^{*}p$ = 0.0222, and $^{***}p$ = 0.0004, one-way ANOVA. (d) FRET ratio images of the GGS17-H3K27me3 biosensor in cells coexpressing wild-type or mutant H3.3. (e) Basal FRET ratios of the GGS17-H3K27me3 biosensor in cells coexpressing wild-type or mutant H3.3. From left to right, n = 48 and 33, with $^{****}p < 0.0001$, Student's t-test (scale bar, 10 μm; error bar, mean ± SD in all figures).

We further constructed a GGS17-H3K27me3 biosensor connected to WT-H3.3 or H3.3M via a P2A cleavage site. After being expressed in the cell, the transgene WT-H3.3 or H3.3M will be cleaved at the P2A site and separated from the GGS17-H3K27me3 biosensor. This strategy can render the same copy number of biosensors and transgene products in a single live cell. Consistent with the previous results, the GGS17-H3K27me3 biosensor can again detect the suppression of H3K27me3 in the H3.3M transduced cells (Figure 3d,e). These results demonstrate the capability of the GGS17-H3K27me3 biosensor in monitoring the epigenetic changes in live cells induced by a histone genetic mutant.

Imaging H3K27me3 in Breast Cancer Cells with Different Genetic Backgrounds. Although MDA-MB-231 and MCF-7 are both breast cancer cell lines, the different genetic backgrounds lead to their differential phenotypes and responses of cells to chemotherapy, with MDA-MB-231 more metastatic and resistant to drugs.[13] Given the crucial role of H3K27me3 in metastasis and resistance,[25−27] we examined whether our GGS17-H3K27me3 biosensor can distinguish these two cell types based on their H3K27me3 levels. We infected both cells with the GGS17-H3K27me3 biosensors and compared the FRET signals. To ensure that the biosensor yields comparable signals in different cells, we compared the level of biosensor expression by quantifying the YPet intensity. There was no significant difference in YPet intensity between MCF-7 and MDA-MB-231 cells, indicating a similar expression level of biosensors in these two cell types (Figure S4). In both the MDA-MB-231 and MCF-7 cell lines, the GGS17-H3K27me3 biosensor has a significantly higher ratio compared to its negative Y26K mutant (Figure 4a−d), confirming the functionality of the biosensor in reporting H3K27me3 levels in both of the breast cancer cell lines. The GGS17-H3K27me3 biosensor showed a significantly higher FRET ratio in the MDA-MB-231 cells than that in the MCF-7 cells (Figure 4e), suggesting a higher H3K27me3 level in MDA-MB-231 cells compared to MCF-7 cells. These results suggest that our GGS17-H3K27me3 biosensor can detect the H3K27me3 difference across cancer cells with different genetic backgrounds.

Tracking of H3K27me3 and Caspase Activity Dynamics in Breast Cancer Cells. Since the epigenetic H3K27me3 has been reported to be involved in the drug resistance of cancer cells[25−27] and closely associated with caspase-3 dependent apoptosis,[24] we utilized our GGS17-H3K27me3 biosensor to investigate the relationship between the caspase-3 activity and H3K27me3 along with the kinetics of these two different molecular events in the same cancer cell during apoptotic processes induced by a kinase inhibitor, e.g., staurosporine. The caspase-3-NES FRET biosensor is adapted from the caspase-3 FRET biosensor developed by Shcherbakova's group.[44] When the caspase-3 enzyme is activated, the DEVD substrate site in between the FRET donor and acceptor in the biosensor is cleaved by caspase-3, leading to the separation of the donor/acceptor pair and the reduction of FRET siganls (Figure 5a). The donor and acceptor FRET pair of long Stokes shift mOrange (LSS-mOrange) and mKate2 in the caspase-3 biosensor is compatible in color with the ECFP−YPet pair of the GGS17-H3K27me3 biosensor, allowing the simultaneous monitoring of both biosensors in the same live cell. Since the caspase-3 activity mainly occurs outside the

https://doi.org/10.1021/acssensors.1c01670
ACS Sens. 2021, 6, 4369−4378

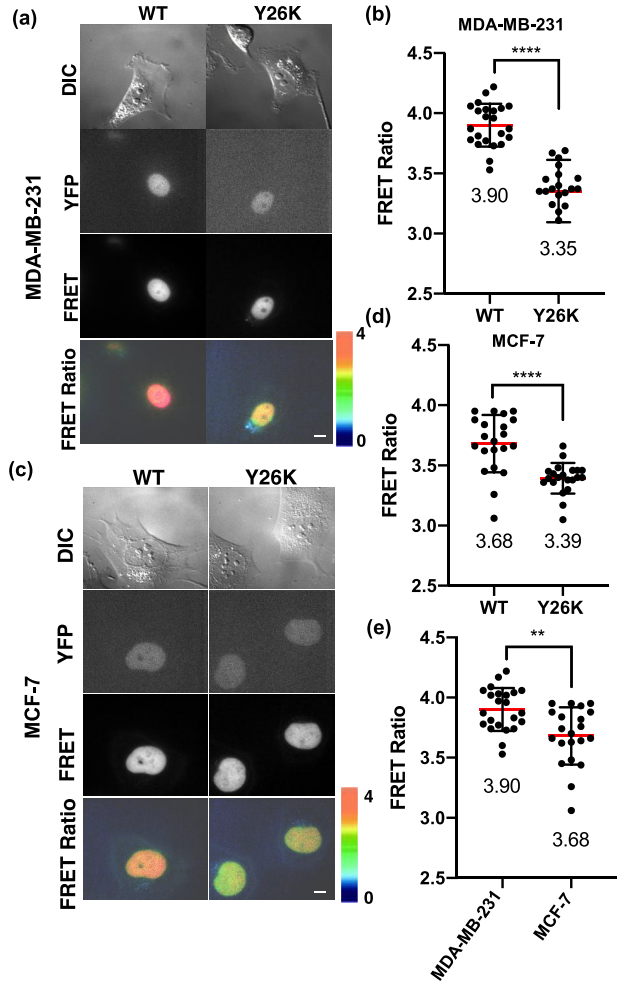

Figure 4. Detecting the H3K27me3 levels in breast cancer cells with different genetic backgrounds. (a,b) Images (a) and basal FRET ratios (b) of the wild-type or mutant (Y26K) GGS17-H3K27me3 biosensors in MDA-MB231 cells. From left to right, n = 23 and 20, with ****p < 0.0001, Student's t-test. (c,d) Images (c) and basal FRET ratios (d) of the wild-type and mutant (Y26K) GGS17-H3K27me3 biosensors in MCF-7 cells. From left to right, n = 21 and 21, with ****p < 0.0001, Student's t-test. (e) Comparison of H3K27me3 between MDA-MB231 and MCF-7 cell lines as detected by the GGS17-H3K27me3 biosensor. From left to right, n = 23 and 21, with **p = 0.0012, Student's t-test (scale bar, 10 μm; error bar, mean ± SD in all figures).

nucleus whereas H3K27me3 activity occurs within the nucleus, a nuclear export signal was added to the C-terminal of the original caspase-3 FRET biosensor (NES-caspase-3 biosensor) to separate the two biosensors and molecular events into the different cellular compartments to further minimize the bleedthrough among different signal channels. When expressed, the newly developed NES-caspase-3 biosensor stayed only in the cytoplasm, while the original caspase biosensor diffused in the whole cell body (Figure S5a). The response time and dynamic change of the NES-caspase-3 biosensor and the original caspase biosensor remained similar (Figure S5b,c). These results suggest that the NES tag can successfully target the caspase-3 biosensor at the subcellular space of the cytoplasm, without imparing its response functions.

To investigate the kinetic coupling between caspase-3 activity and H3K27me3 in cancer cells, we further infected HeLa cancer cells with GGS17-H3K27me3 and NES-caspase-3 FRET biosensors. The initiation of the apoptotic process in the cancer cells upon staurosporine treatment, represented by the change of the NES-caspase-3 FRET biosensor, was found to occur significantly earlier than the decrease in H3K27me3 reported by the GGS17-H3K27me3 biosensor. To further confirm the histone demethylation, we performed immunofluorescence staining to quantify the H3K27me3 biochemically during apoptosis. Since the median time of demethylation measured by the FRET assay in HeLa cells upon staurosporine treatment is 250 min, we analyzed the H3K27me3 level of the cells after 4 h (240 min) of staurosporine treatment (Figure S6a). The immunofluorescence staining results showed significant demethylation of H3K27me3 in HeLa cells, consistent with the results as reported by the FRET biosensor (Figure S6b,c). Furthermore, the median time difference (Δt) between the starting time of the decrease in the caspase-3 FRET ratio (t_C) and that of H3K27me3 (t_H) in 34 cells is at 100 min, suggesting that the protease caspase-3 cleavage actions in the cytoplasm occur significantly earlier than the epigenetic H3K27me3 alteration in the nucleus in staurosporine-induced apoptotic processes in cancer cells (Figure 5b−d). To quantitatively evaluate the relationship between H3K27me3 and caspase activities, we used the temporal cross-correlation of caspase-3 activity and H3K27me3, which integrates the time course data from multiple cells to assess the kinetic coupling of these two molecular events despite heterogeneous signaling among different cells (Figure 5e). The correlation coefficient between the changes of caspase-3 activity and H3K27me3 is high at 0.736, indicating a high association and kinetic coupling of these two signaling events. In contrast, the correlation coefficient between the signals of caspase-3 activity and the control negative H3K27me3 biosensor with the Y26K mutation has a significantly lower value, suggesting that the detected coupling between caspase-3 and H3K27me3 is biologically specific but not due to nonspecific morphological changes (Figure 5e). In summary, by combining the color-compatible GGS17-H3K27me3 and NES-caspase-3 FRET biosensors, the dynamic changes of protease caspase-3 activity and epigenetic H3K27me3 were simultaneously visualized and quantified during the apoptotic process in the same live cancer cells. These results should lead to our in-depth understanding of molecular coordinations in cancer cells in response to drug treatment.

DISCUSSION

In this work, we have developed a FRET biosensor capable of visualizing the dynamic changes of H3K27me3, a key epigenetic and chromatin signal related to the local repression of genes. We have systematically changed the linkers in the biosensor to improve the specificity. It is clear that the primary linker between the FRET donor and acceptor, in this case, ECFP and YPet, is important for the overall FRET levels. The shorter primary linkers produce stronger FRET signals (Figure 2g), presumably by allowing a higher probability for the donor and acceptor to form a favorable distance/orientation for FRET when the histone tail is trimethylated at the H3K27 residue, overcoming the relative weak binding affinity of the Pc domain toward H3K27me3.[41] This higher level of overall FRET signals also leads to a larger dynamic range of the biosensor between its nonmethylated and methylated states. It should be noted that the 15-mer GGS linker between Pc and YPet in our biosensor also caused a better dynamic range, possibly by allowing a more flexible orientation to result in a

https://doi.org/10.1021/acssensors.1c01670
ACS Sens. 2021, 6, 4369−4378

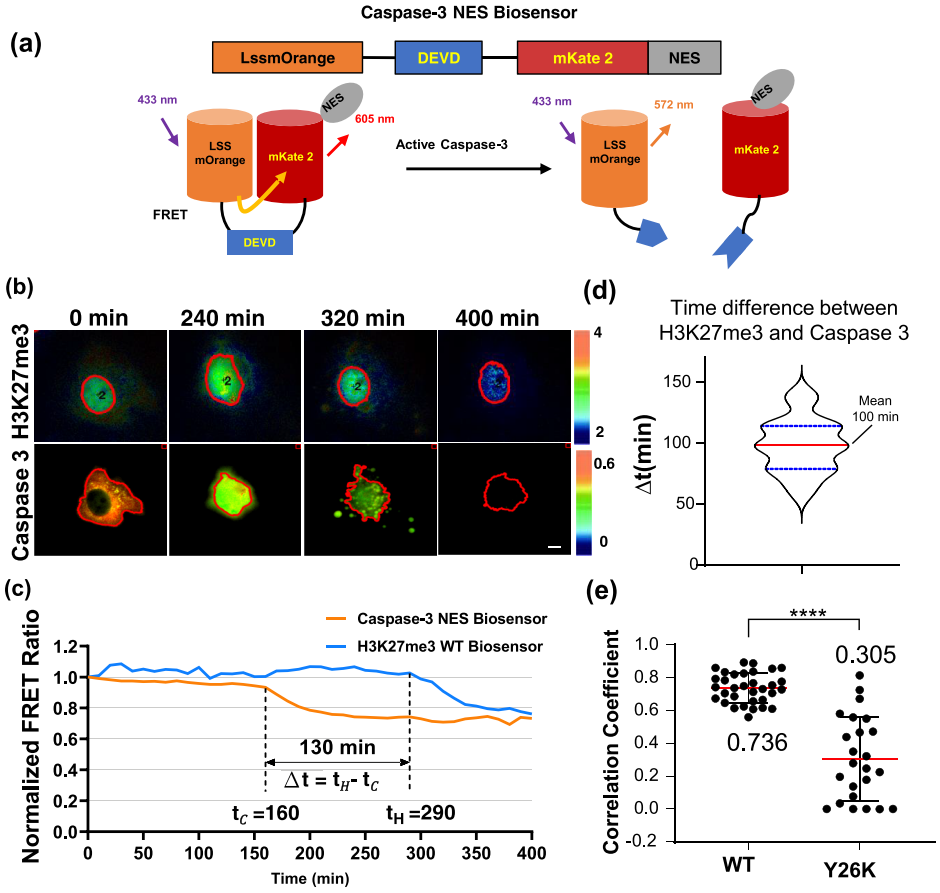

Figure 5. Development and integration of the caspase-3-NES biosensor for the visualization of dynamic coordination between H3K27me3 and caspase-3. (a) Schematic drawing of the NES-tagged caspase-3 FRET biosensor and the proposed activation mechanism. (b,c) Images (b) and time courses (c) of FRET ratio changes of the caspase-3-NES biosensor and the GGS17-H3K27me3 biosensor in the same HeLa cells. (d) Time lag between the FRET ratio decreases of caspase-3 and those of H3K27me3. The median time (100 min) is represented by the red line, and the upper and lower quartile is represented by the blue dashed lines. $n = 34$. (e) Comparison of the correlation coefficients calculated between the caspase-3-NES biosensor and the wild-type or mutant (Y26K) GGS17-H3K27me3 biosensors. From left to right, $n = 33$ and 24, with ****$p < 0.0001$, Student's t-test (scale bar, 10 μm; error bar, mean ± SD in all figures).

higher FRET signal facilitated by the dimerization tendency of ECFP and YPet when histone methylation occurs. The polycomb (Pc) chromodomain used in this study has been demonstrated to have high specificity (K_d = 5 μM) to the trimethyl-Lys 27 H3, as shown in previous studies.[41,45] Since there are about 30 million copies of nucleosomes and H3 tails in the nucleus before the genome duplication and the integration of the biosensor into nucleosomes is rather random, the Pc domain in the biosensor carrying the histone peptide mutant may interact with the adjacent trimethyl-Lys 27 residues of the endogenous histone tails. In contrast, the disruption of the Pc domain via Y26K mutation can abolish the interactions of the Pc domain with the biosensor as well as native histone peptides. This difference between the histone peptide mutant and the Pc domain mutant of the biosensor may have led to a higher basal FRET ratio in the histone peptide mutant than the Pc domain mutant of the biosensor (Figure 2h). With this combined engineering effort on multiple linkers, the final GGS17-H3K27me3 biosensor had an ∼43% change between the "on" and "off" states, whereas the prototype biosensor only had an ∼13% change. It is of note that the FRET-based images can have differences from the antibody-based immunostaining data (Figure S3). The antibody staining may lead to false-positive signals where the chromatin is condensed with multiple copies of histone tails even when these histone tails are not highly methylated. In contrast, the intensity-modulated display (IMD) images of FRET signals are based on the ratiometric calculation of FRET/ECFP. With each biosensor containing one donor and one acceptor, this acceptor/donor ratiometric calculation can eliminate the noise engendered from the copy number difference of the biosensors at different subnuclear regions and hence can reflect more precisely the histone methyltransferase activities but not the copy number of histone tails in the local areas.

The GGS17-H3K27me3 biosensor enables the detection of H3K27me3 changes induced by the genetic H3.3K27M mutation and the comparison of H3K27me3 levels in breast cancer subtypes with different genetic backgrounds in single live cells. Specifically, the drug-resistant and metastatic triple-negative MDA-MB-231 cells were found to have a higher level of H3K27me3 than the less invasive HER2$^+$ MCF-7 cells. Furthermore, together with a caspase biosensor, we achieved multicolor imaging of two molecular events, namely, caspase activity and H3K27me3 modulations, simultaneously in the same live cells. Our results revealed that when staurosporine was applied to treat cancer cells, caspase activation occurs first in the cytoplasm to trigger apoptosis followed by a delayed

https://doi.org/10.1021/acssensors.1c01670
ACS Sens. 2021, 6, 4369−4378

H3K27me3 reduction in the nucleus. Intriguingly, there is an average of an around 100 min gap between the activation of caspase-3 and H3K27me3 measured in the same live cells. We reasoned that this occurs because there are multiple steps of molecular actions in between these two events. The actions of caspase-3 may trigger an accumulative effect until it reaches a threshold to cause the ultimate change of the epigenetic H3K27 methylations, which eventually lead to cell death. Based on our results, the wild-type biosensor showed a significant reduction of the FRET ratio compared to the loss of function mutant (Y26K) biosensors in the FRET assay after 4 h of staurosporine treatment (Figure S7), which demonstrated that the WT biosensor indeed has the specificity in detecting the demethylation in the apoptotic cells. In addition, it was reported that the degradation of histone after high-concentration staurosporine (1 M) treatment happens after 24 h,[46] which occurs much later than our detecting point (2.5 μM, 4 h). Nevertheless, we cannot entirely rule out the possibility that the observed demethylation of the apoptotic cells may be due to the degradation of histones, fragmentation of DNA, or global changes in chromatin organization.

Epigenetic histone modifications play a crucial role in regulating genomic coordination, cellular functions, and subsequently various pathophysiological processes.[2] H3K27me3 is generally considered a repressive motif for gene expressions. Emerging evidence indicates that overexpression of the H3K27me3 methyltransferase EZH2 is highly indicative of pancreatic cancer progression.[47,48] Global-level EZH2 inhibition decreases pancreatic cancer cell migration and sensitizes the cellular response toward the chemotherapeutic gemcitabine.[47−50] On the other hand, low levels of H3K27me3, or the loss of H3K27me3, have been associated with poor prognosis in breast, ovarian, and pancreatic cancers.[15] These seemingly contradictory reports on H3K27me3 and their corresponding methyltransferases probably reflect the highly complex and heterogeneous nature of cancer cells. In this study, a significant reduction of the H3K27me3 level was found in HeLa cells in the FRET assay with the WT biosensor (Figure 5b,c) and immunofluorescence staining assay (Figure S6b,c). Meanwhile, these results were in line with a previous study showing that staurosporine treatment could reduce the H3K27me3 level in multiple cancer cells after 2 h of treatment using a Western blot assay.[51] However, in another study, the authors reported that trimethylation of H3K27 was induced by staurosporine (1 μM, 3 h) in G292 cells, a human osteosarcoma cell line, which is different from our findings. It is possible that the influence of the drugs on histone methylation may have dose- or cell-specific responses, possibly due to the difference in genetic backgrounds. Future studies could focus on the spatiotemporal characteristics of H3K27me3 in different cell lines under apoptosis. Thus, our H3K27me3 biosensor can be a crucial tool to reveal the dynamic and subcellular H3K27me3 status in these live cells. We can foresee that integrating live-cell locus-specific labeling tools[52] with our nucleosome-integrated FRET biosensors would further provide the genomic locus-specific and dynamic epigenetic changes in single live cells. This biosensor can also be applied to visualize and quantify the epigenetic adaptation of drug resistance responses in cancer cells as well as support the live-cell screening of inhibitors with high precision for their therapeutic efficacy.

MATERIALS AND METHODS

Construction of the H3K27me3 and Caspase-3-NES FRET Biosensors. The cDNA of the truncated polycomb domain was generated by PCR using the pcDNA3-K27 histone methylation reporter (Addgene, cat. no. 22865) as a template, and the EV-linker-ECFP-H3 fragment was generated by PCR using the pCBI-H3K9me3 biosensor from our group as a template. The two fragments were assembled into a pcDNA3.1+ vector (Thermo Fisher Scientific) via Gibson assembly using the Gibson Assembly Master Mix (New England BioLabs) to generate the prototype wild-type H3K27me3 biosensor. A short 45 base pair linker 3′-GGGTCTACATCTG-GATCTGGGAAGCCGGGTTCTGGTGAGGGTTCT-3′ purchased from IDT gBlocks Gene Fragment was inserted after the polycomb domain and before YPet to make the GGS-linker prototype H3K27me3 biosensor via Gibson assembly. Point mutations of K27L, K27M on full-length H3, and Y26K on the truncated polycomb domain were introduced into both the prototype H3K27me3 biosensor and the GGS-linker prototype H3K27me3 biosensor using a Q5 site-directed mutagenesis kit (New England BioLabs).

The YPet-Pc swapped H3K27me3 wild-type or mutant biosensors were created by swapping the YPet and the truncated polycomb domain on the prototype wild-type or mutant H3K27me3 biosensors through PCR and Gibson assembly. The 34-mer linker 5′-GSTSGSGKPGSGEGSTKGSTSGSGKPGSGEGSTK-3′ and the 17-mer linker 5′-GSTSGSGKPGSGEGSTK-3′ were synthesized in IDT's gBlocks Gene Fragment and replaced the EV linker in the GGS-linker prototype biosensors via Gibson assembly to produce 34-mer linker biosensors and 17-mer linker biosensors. The nuclear export signal sequence 5′TTAGCCTTGAAATTAGCAGGTCTTGATATCGG-GAGC-3′ was cloned into a caspase-3 biosensor (Addgene, Cat #60883) by PCR and ligation.

Cell Culture and Transfection. HEK 293T, MDA-MB-231, MCF-7, and HeLa cells were cultured in high-glucose, pyruvate-supplemented Dulbecco's modified Eagle medium (Life Technologies Corporation) with 10% (vol/vol) heat-inactivated fetal bovine serum (Life Technologies Corporation) and 100 units/mL penicillin−streptomycin (Thermo Fisher Scientific) at 1 atm and 37 °C with 5% CO_2. Cell transfection with plasmid DNAs was performed using lipofectamine 3000 (Invitrogen) following the manufacturer's instructions.

Lentiviral Infection. The lentivirus of biosensors and transgenes were cotransfected with pCMV-ΔR and pCMV-VSVG plasmids into HEK 293T cells at 70% confluency using a ProFection mammalian transfection system (Promega) following the manufacturer's instructions. 48−72 h after transfection, the viral supernatant was harvested, filtered through a 0.45 μm polyethersulfone filter, and concentrated to 100× using PEG-it virus precipitation solution (System Biosciences) before use. HEK cells and Hela cells were incubated with a virus-containing medium for 48−72 h during viral infection. Cells were then incubated in 1 μg/mL puromycin for 24−72 h for selection and passaged into the complete medium before imaging or immunoblotting.

Image Acquisition and Analysis. Cells were plated onto glass-bottom dishes (Cell E&G) coated with fibronectin (Sigma) diluted with PBS at 10 μg/mL one night before imaging. In the caspase-3-NES biosensor coupled experiment, staurosporine (Cell Signaling, cat. no. 9953) was added to the cell at 20 min at a final concentration of 2 μM.

A Nikon Eclipse Ti inverted microscope with a 100× DIC Nikon microscope objective (numerical aperture, 1.4), a 300 W xenon lamp (Atlas Specialty Lighting), an electron-multiplying (EM) charge-coupled device camera (QuantEM:512SC, Photometrics), and MetaFluor fluorescence ratio imaging software (Molecular Devices) was used to collect microscopic images. Images were captured with a 420DF20 excitation filter, a 450DRLP dichroic mirror, and four emission filters controlled by a filter changer corresponding with four channels (475DF40 for ECFP, 535DF25 for ECFP−YPet FRET, 575DF20 for LSSmOrange, and 630DF20 for LSSmOrange-mKate2 FRET). For dual FRET imaging with single-wavelength excitation, the

https://doi.org/10.1021/acssensors.1c01670
ACS Sens. 2021, 6, 4369−4378

images of LSSmOrange-mKate2 channels were collected with an exposure time of 400 ms and those of ECFP−YPet channels at 600 ms. The whole duration of imaging for a single cell was about 500 min with a time interval of 10 min.

Imaging data were processed on JAVA-MATLAB-based Fluocell developed by our lab.[53] The background and noise signals were subtracted automatically by Fluocell before further analysis. The FRET ratio is an average value for a whole cell and normalized by the first frame value ($t = 0$).

Quantification and Cross-Correlation Analysis. In signal processing, the cross-correlation function is a measurement of similarity between two dynamics signals when there is a time lag between them. The discrete cross-correlation function (CC) between the signals A and B (A−B CC curve) is defined by the following equation:

$$\mathrm{CC}(A, B, k) = \frac{\sum_{i=1}^{n} A(i)B(i+k)}{\left(\sum_{i=1}^{n} A(i)^2\right)^{1/2}\left(\sum_{i=1}^{n} B(i)^2\right)^{1/2}}$$

where

$$k = \{-m, -(m-1), \ldots, -3, -2, -1, 0, 1, 2, 3, \ldots, m-1, m\}, m < n,$$

$$A = \{A(1), A(2), \ldots, A(n)\}, \text{ and}$$

$$B = \{B(-(m-1)), B(-(m-2)), \ldots, B(0), B(1), B(2), \ldots, B(n), B(n+1), \ldots, B(n+k)\}.$$

In this study, the cross-correlation function was used to compare the trend and the similarity of two biosensors' signals within one cell. Our customized Fluocell cross-correlation function was used instead of the MATLAB functions xcorr or xcov. The MATLAB functions extend the A and B signals to both sides using the value zero. The Fluocell cross-correlation function extends the signals by their end value at both sides, which accurately captures the dynamic characteristics of the FRET biosensor signals. In addition, both signals were normalized such that the maximal value of the autocorrelation function is 1. The average cross-correlation coefficients can be computed based on the values of CC curves from different cells.[54]

Immunoblotting Analysis. HEK cells infected with H3.3WT and H3.3M viruses were cultured in 1 μg/mL puromycin for 72 h and then in a complete medium for one week before protein extraction. Histone proteins of infected H3.3WT and H3.3M cells were extracted using a histone extraction kit (Abcam) following the manufacturer's protocol. Immunoblotting analysis was performed using a Mini-PROTEAN TGX precast protein gel (Bio-rad) following the manufacturer's standard protocol using an anti-H3K27me3 antibody (Cell Signaling C36B11), an anti-DDDDK tag antibody (Abcam, ab1162), and an antihistone H3 antibody (Abcam, ab1791) as primary antibodies and goat anti-rabbit IgG-HRP (Santa Cruz, sc-2004) as the secondary antibody. Immunoblotting was finally visualized using a SuperSignal West Pico PLUS chemiluminescent substrate (Thermo Fisher).

Statistical Analysis. Statistical analyses and figures drawing were performed using GraphPad Prism version 6, Matlab R2019b, or Excel. Pairwise comparisons were performed using Student's t-test. Comparisons between more than two groups were performed using one-way ANOVA as indicated in the figure legends. The sample size, statistical significance value, and error bar graphs were listed in figures or figure legends.

■ ASSOCIATED CONTENT

Supporting Information

The Supporting Information is available free of charge at https://pubs.acs.org/doi/10.1021/acssensors.1c01670.

Supplementary figures: images of control biosensors, spatial distribution of H3K27me3 in the nucleus, quantification of biosensor expression in different cell types, characterization of the caspase-3-NES biosensor, and verification of H3K27 demethylation during apoptosis (PDF)

■ AUTHOR INFORMATION

Corresponding Authors

Longwei Liu − *Department of Bioengineering, Institute of Engineering in Medicine, University of California, San Diego, La Jolla, California 92093-0435, United States*; Email: lol001@eng.ucsd.edu

Yingxiao Wang − *Department of Bioengineering, Institute of Engineering in Medicine, University of California, San Diego, La Jolla, California 92093-0435, United States*; orcid.org/0000-0003-0265-326X; Email: yiw015@eng.ucsd.edu

Authors

Ya Gong − *Department of Bioengineering, Institute of Engineering in Medicine, University of California, San Diego, La Jolla, California 92093-0435, United States*

Chujun Wei − *Department of Bioengineering, Institute of Engineering in Medicine, University of California, San Diego, La Jolla, California 92093-0435, United States*

Leonardo Cheng − *Department of Bioengineering, Institute of Engineering in Medicine, University of California, San Diego, La Jolla, California 92093-0435, United States*

Fengyi Ma − *Department of Bioengineering, Institute of Engineering in Medicine, University of California, San Diego, La Jolla, California 92093-0435, United States*

Shaoying Lu − *Department of Bioengineering, Institute of Engineering in Medicine, University of California, San Diego, La Jolla, California 92093-0435, United States*

Qin Peng − *Department of Bioengineering, Institute of Engineering in Medicine, University of California, San Diego, La Jolla, California 92093-0435, United States*

Complete contact information is available at: https://pubs.acs.org/10.1021/acssensors.1c01670

Author Contributions

Y.G., C.W., and Y.W. designed the research; Y.G. and C.W. performed the research; Y.G., C.W., F.M., L.C., L.L., and S.L. analyzed the data; Q.P. provided new reagents/analytic tools; Y.G., C.W., L.L., and Y.W. wrote the paper. All authors reviewed the manuscript.

Notes

The authors declare the following competing financial interest(s): Yingxiao Wang and Shaoying Lu are scientific co-founders of Cell E&G Inc. However, these financial interests do not affect the design, conduct or reporting of this research.

■ ACKNOWLEDGMENTS

This work is supported by grants from NIH HL121365, EB029122, GM140929, and GM126016 (Y.W.). The funding agencies had no role in study design, data collection and analysis, decision to publish, or preparation of the manuscript.

REFERENCES

(1) Bannister, A. J.; Kouzarides, T. Regulation of chromatin by histone modifications. *Cell Res.* **2011**, *21*, 381−395.
(2) Ng, S. S.; Yue, W. W.; Oppermann, U.; Klose, R. J. Dynamic protein methylation in chromatin biology. *Cell. Mol. Life Sci.* **2009**, *66*, 407−422.
(3) Wen, K. X.; Milic, J.; El-Khodor, B.; Dhana, K.; Nano, J.; Pulido, T.; Kraja, B.; Zaciragic, A.; Bramer, W. M.; Troup, J.; Chowdhury, R.; Ikram, M. A.; Dehghan, A.; Muka, T.; Franco, O. H. The Role of DNA Methylation and Histone Modifications in Neurodegenerative Diseases: A Systematic Review. *PLoS One* **2016**, *11*, No. e0167201.
(4) Guenatri, M.; Bailly, D.; Maison, C.; Almouzni, G. Mouse centric and pericentric satellite repeats form distinct functional heterochromatin. *J. Cell. Biol.* **2004**, *166*, 493−505.
(5) Peterson, C. L.; Laniel, M. A. Histones and histone modifications. *Curr. Biol.* **2004**, *14*, R546−R551.
(6) Margueron, R.; Reinberg, D. The Polycomb complex PRC2 and its mark in life. *Nature* **2011**, *469*, 343−349.
(7) Varambally, S.; Dhanasekaran, S. M.; Zhou, M.; Barrette, T. R.; Kumar-Sinha, C.; Sanda, M. G.; Ghosh, D.; Pienta, K. J.; Sewalt, R. G. A. B.; Otte, A. P.; Rubin, M. A.; Chinnaiyan, A. M. The polycomb group protein EZH2 is involved in progression of prostate cancer. *Nature* **2002**, *419*, 624−629.
(8) Krill, L.; Deng, W.; Eskander, R.; Mutch, D.; Zweizig, S.; Hoang, B.; Ioffe, O.; Randall, L.; Lankes, H.; Miller, D. S.; Birrer, M. Overexpression of enhance of Zeste homolog 2 (EZH2) in endometrial carcinoma: An NRG Oncology/Gynecologic Oncology Group Study. *Gynecol Oncol* **2020**, *156*, 423−429.
(9) Chan, K. M.; Fang, D.; Gan, H.; Hashizume, R.; Yu, C.; Schroeder, M.; Gupta, N.; Mueller, S.; James, C. D.; Jenkins, R.; Sarkaria, J.; Zhang, Z. The histone H3.3K27M mutation in pediatric glioma reprograms H3K27 methylation and gene expression. *Genes Dev.* **2013**, *27*, 985−990.
(10) Bachmann, I. M.; Halvorsen, O. J.; Collett, K.; Stefansson, I. M.; Straume, O.; Haukaas, S. A.; Salvesen, H. B.; Otte, A. P.; Akslen, L. A. EZH2 expression is associated with high proliferation rate and aggressive tumor subgroups in cutaneous melanoma and cancers of the endometrium, prostate, and breast. *J. Clin. Oncol.* **2006**, *24*, 268−273.
(11) Lewis, P. W.; Muller, M. M.; Koletsky, M. S.; Cordero, F.; Lin, S.; Banaszynski, L. A.; Garcia, B. A.; Muir, T. W.; Becher, O. J.; Allis, C. D. Inhibition of PRC2 activity by a gain-of-function H3 mutation found in pediatric glioblastoma. *Science* **2013**, *340*, 857−861.
(12) Chavez, K. J.; Garimella, S. V.; Lipkowitz, S. Triple negative breast cancer cell lines: one tool in the search for better treatment of triple negative breast cancer. *Breast Dis.* **2010**, *32*, 35−48.
(13) Osborne, C. K. Tamoxifen in the treatment of breast cancer. *N. Engl. J. Med.* **1998**, *339*, 1609−1618.
(14) Holm, K.; Grabau, D.; Lövgren, K.; Aradottir, S.; Gruvberger-Saal, S.; Howlin, J.; Saal, L. H.; Ethier, S. P.; Bendahl, P.-O.; Stål, O.; Malmström, P.; Fernö, M.; Rydén, L.; Hegardt, C.; Borg, Å.; Ringnér, M. Global H3K27 trimethylation and EZH2 abundance in breast tumor subtypes. *Mol. Oncol.* **2012**, *6*, 494−506.
(15) Wei, Y.; Xia, W.; Zhang, Z.; Liu, J.; Wang, H.; Adsay, N. V.; Albarracin, C.; Yu, D.; Abbruzzese, J. L.; Mills, G. B.; Bast, R. C., Jr.; Hortobagyi, G. N.; Hung, M. C. Loss of trimethylation at lysine 27 of histone H3 is a predictor of poor outcome in breast, ovarian, and pancreatic cancers. *Mol. Carcinog.* **2008**, *47*, 701−706.
(16) Zsindely, N.; Bodai, L. Histone methylation in Huntington's disease: are bivalent promoters the critical targets? *Neural Regener. Res.* **2018**, *13*, 1191−1192.
(17) Mohammad, R. M.; Muqbil, I.; Lowe, L.; Yedjou, C.; Hsu, H.-Y.; Lin, L.-T.; Siegelin, M. D.; Fimognari, C.; Kumar, N. B.; Dou, Q. P.; Yang, H.; Samadi, A. K.; Russo, G. L.; Spagnuolo, C.; Ray, S. K.; Chakrabarti, M.; Morre, J. D.; Coley, H. M.; Honoki, K.; Fujii, H.; Georgakilas, A. G.; Amedei, A.; Niccolai, E.; Amin, A.; Ashraf, S. S.; Helferich, W. G.; Yang, X.; Boosani, C. S.; Guha, G.; Bhakta, D.; Ciriolo, M. R.; Aquilano, K.; Chen, S.; Mohammed, S. I.; Keith, W. N.; Bilsland, A.; Halicka, D.; Nowsheen, S.; Azmi, A. S. Broad targeting of resistance to apoptosis in cancer. *Semin. Cancer Biol.* **2015**, *35*, S78−S103.
(18) Johnstone, R. W.; Ruefli, A. A.; Lowe, S. W. Apoptosis: a link between cancer genetics and chemotherapy. *Cell* **2002**, *108*, 153−164.
(19) Lekshmi, A.; Varadarajan, S. N.; Lupitha, S. S.; Indira, D.; Mathew, K. A.; Chandrasekharan Nair, A.; Nair, M.; Prasad, T.; Sekar, H.; Gopalakrishnan, A. K.; Murali, A.; Santhoshkumar, T. R. A quantitative real-time approach for discriminating apoptosis and necrosis. *Cell Death Discovery* **2017**, *3*, 16101.
(20) Cheung, W. L.; Ajiro, K.; Samejima, K.; Kloc, M.; Cheung, P.; Mizzen, C. A.; Beeser, A.; Etkin, L. D.; Chernoff, J.; Earnshaw, W. C.; Allis, C. D. Apoptotic phosphorylation of histone H2B is mediated by mammalian sterile twenty kinase. *Cell* **2003**, *113*, 507−517.
(21) Hurd, P. J.; Bannister, A. J.; Halls, K.; Dawson, M. A.; Vermeulen, M.; Olsen, J. V.; Ismail, H.; Somers, J.; Mann, M.; Owen-Hughes, T.; Gout, I.; Kouzarides, T. Phosphorylation of histone H3 Thr-45 is linked to apoptosis. *J. Biol. Chem.* **2009**, *284*, 16575−16583.
(22) Cheng, M. F.; Lee, C. H.; Hsia, K. T.; Huang, G. S.; Lee, H. S. Methylation of histone H3 lysine 27 associated with apoptosis in osteosarcoma cells induced by staurosporine. *Histol. Histopathol.* **2009**, *24*, 1105−1111.
(23) Kim, K. H.; Roberts, C. W. M. Targeting EZH2 in cancer. *Nat. Med.* **2016**, *22*, 128−134.
(24) Wu, Z. L.; Zheng, S. S.; Li, Z. M.; Qiao, Y. Y.; Aau, M. Y.; Yu, Q. Polycomb protein EZH2 regulates E2F1-dependent apoptosis through epigenetically modulating Bim expression. *Cell Death Differ.* **2010**, *17*, 801−810.
(25) He, C.; Sun, J.; Liu, C.; Jiang, Y.; Hao, Y. Elevated H3K27me3 levels sensitize osteosarcoma to cisplatin. *Clin. Epigenet.* **2019**, *11*, 8.
(26) Zhao, F.; Chen, Y.; Li, R.; Liu, Y.; Wen, L.; Zhang, C. Triptolide alters histone H3K9 and H3K27 methylation state and induces G0/G1 arrest and caspase-dependent apoptosis in multiple myeloma in vitro. *Toxicology* **2010**, *267*, 70−79.
(27) Zhao, F.; Chen, Y.; Zeng, L.; Li, R.; Zeng, R.; Wen, L.; Liu, Y.; Zhang, C. Role of triptolide in cell proliferation, cell cycle arrest, apoptosis and histone methylation in multiple myeloma U266 cells. *Eur. J. Pharmacol.* **2010**, *646*, 1−11.
(28) Noma, K. I.; Allis, C. D.; Grewal, S. I. S. Transitions in distinct histone H3 methylation patterns at the heterochromatin domain boundaries. *Science* **2001**, *293*, 1150−1155.
(29) Sanchez, O. F.; Mendonca, A.; Carneiro, A. D.; Yuan, C. Engineering Recombinant Protein Sensors for Quantifying Histone Acetylation. *ACS Sens.* **2017**, *2*, 426−435.
(30) Mendonca, A.; Sánchez, O. F.; Xie, J.; Carneiro, A.; Lin, L.; Yuan, C. Identifying distinct heterochromatin regions using combinatorial epigenetic probes in live cells. *Biochim. Biophys. Acta, Gene Regul. Mech.* **2021**, *1864*, 194725.
(31) Lungu, C.; Pinter, S.; Broche, J.; Rathert, P.; Jeltsch, A. Modular fluorescence complementation sensors for live cell detection of epigenetic signals at endogenous genomic sites. *Nat. Commun.* **2017**, *8*, 649.
(32) Wang, Y.; Shyy, J.-Y.; Chien, S. Fluorescence proteins, live-cell imaging, and mechanobiology: seeing is believing. *Annu. Rev. Biomed. Eng.* **2008**, *10*, 1−38.
(33) Greenwald, E. C.; Mehta, S.; Zhang, J. Genetically Encoded Fluorescent Biosensors Illuminate the Spatiotemporal Regulation of Signaling Networks. *Chem. Rev.* **2018**, *118*, 11707−11794.
(34) Zhang, J. F.; Mehta, S.; Zhang, J. Signaling Microdomains in the Spotlight: Visualizing Compartmentalized Signaling Using Genetically Encoded Fluorescent Biosensors. *Annu. Rev. Pharmacol. Toxicol.* **2021**, *61*, 587−608.
(35) Miyawaki, A. Visualization of the spatial and temporal dynamics of intracellular signaling. *Dev. Cell* **2003**, *4*, 295−305.
(36) Aoki, K.; Kiyokawa, E.; Nakamura, T.; Matsuda, M. Visualization of growth signal transduction cascades in living cells with genetically encoded probes based on Forster resonance energy transfer. *Philos. Trans. R. Soc., B* **2008**, *363*, 2143−2151.

https://doi.org/10.1021/acssensors.1c01670
ACS Sens. 2021, 6, 4369−4378

(37) Sasaki, K.; Ito, T.; Nishino, N.; Khochbin, S.; Yoshida, M. Real-time imaging of histone H4 hyperacetylation in living cells. *Proc. Natl. Acad. Sci.* **2009**, *106*, 16257−16262.
(38) Ito, T.; Umehara, T.; Sasaki, K.; Nakamura, Y.; Nishino, N.; Terada, T.; Shirouzu, M.; Padmanabhan, B.; Yokoyama, S.; Ito, A.; Yoshida, M. Real-time imaging of histone H4K12-specific acetylation determines the modes of action of histone deacetylase and bromodomain inhibitors. *Chem. Biol.* **2011**, *18*, 495−507.
(39) Lin, C. W.; Jao, C. Y.; Ting, A. Y. Genetically encoded fluorescent reporters of histone methylation in living cells. *J. Am. Chem. Soc.* **2004**, *126*, 5982−5983.
(40) Peng, Q.; Lu, S.; Shi, Y.; Pan, Y.; Limsakul, P.; Chernov, A. V.; Qiu, J.; Chai, X.; Shi, Y.; Wang, P.; Ji, Y.; Li, Y. J.; Strongin, A. Y.; Verkhusha, V. V.; Izpisua Belmonte, J. C.; Ren, B.; Wang, Y.; Chien, S.; Wang, Y. Coordinated histone modifications and chromatin reorganization in a single cell revealed by FRET biosensors. *Proc. Natl. Acad. Sci. U. S. A.* **2018**, *115*, E11681−E11690.
(41) Fischle, W.; Wang, Y.; Jacobs, S. A.; Kim, Y.; Allis, C. D.; Khorasanizadeh, S. Molecular basis for the discrimination of repressive methyl-lysine marks in histone H3 by Polycomb and HP1 chromodomains. *Genes Dev.* **2003**, *17*, 1870−1881.
(42) Gonzalez-Vera, J. A. Probing the kinome in real time with fluorescent peptides. *Chem. Soc. Rev.* **2012**, *41*, 1652−1664.
(43) Whitlow, M.; Bell, B. A.; Feng, S. L.; Filpula, D.; Hardman, K. D.; Hubert, S. L.; Rollence, M. L.; Wood, J. F.; Schott, M. E.; Milenic, D. E.; et al. An improved linker for single-chain Fv with reduced aggregation and enhanced proteolytic stability. *Protein Eng.* **1993**, *6*, 989−995.
(44) Shcherbakova, D. M.; Hink, M. A.; Joosen, L.; Gadella, T. W.; Verkhusha, V. V. An orange fluorescent protein with a large Stokes shift for single-excitation multicolor FCCS and FRET imaging. *J. Am. Chem. Soc.* **2012**, *134*, 7913−7923.
(45) Min, J.; Zhang, Y.; Xu, R. M. Structural basis for specific binding of Polycomb chromodomain to histone H3 methylated at Lys 27. *Genes Dev.* **2003**, *17*, 1823−1828.
(46) Lee, P. Y.; Park, B. C.; Chi, S. W.; Bae, K.-H.; Kim, S.; Cho, S.; Kang, S.; Kim, J.-H.; Park, S. G. Histone H4 is cleaved by granzyme A during staurosporine-induced cell death in B-lymphoid Raji cells. *BMB Rep.* **2016**, *49*, 560−565.
(47) Varambally, S.; Cao, Q.; Mani, R. S.; Shankar, S.; Wang, X.; Ateeq, B.; Laxman, B.; Cao, X.; Jing, X.; Ramnarayanan, K.; Brenner, J. C.; Yu, J.; Kim, J. H.; Han, B.; Tan, P.; Kumar-Sinha, C.; Lonigro, R. J.; Palanisamy, N.; Maher, C. A.; Chinnaiyan, A. M. Genomic loss of microRNA-101 leads to overexpression of histone methyltransferase EZH2 in cancer. *Science* **2008**, *322*, 1695−1699.
(48) McCabe, M. T.; Ott, H. M.; Ganji, G.; Korenchuk, S.; Thompson, C.; Van Aller, G. S.; Liu, Y.; Graves, A. P.; Della Pietra, A., 3rd; Diaz, E.; LaFrance, L. V.; Mellinger, M.; Duquenne, C.; Tian, X.; Kruger, R. G.; McHugh, C. F.; Brandt, M.; Miller, W. H.; Dhanak, D.; Verma, S. K.; Tummino, P. J.; Creasy, C. L. EZH2 inhibition as a therapeutic strategy for lymphoma with EZH2-activating mutations. *Nature* **2012**, *492*, 108−112.
(49) Avan, A.; Crea, F.; Paolicchi, E.; Funel, N.; Galvani, E.; Marquez, V. E.; Honeywell, R. J.; Danesi, R.; Peters, G. J.; Giovannetti, E. Molecular mechanisms involved in the synergistic interaction of the EZH2 inhibitor 3-deazaneplanocin A with gemcitabine in pancreatic cancer cells. *Mol. Cancer Ther.* **2012**, *11*, 1735−1746.
(50) Cao, Q.; Yu, J.; Dhanasekaran, S. M.; Kim, J. H.; Mani, R. S.; Tomlins, S. A.; Mehra, R.; Laxman, B.; Cao, X.; Kleer, C. G.; Varambally, S.; Chinnaiyan, A. M. Repression of E-cadherin by the polycomb group protein EZH2 in cancer. *Oncogene* **2008**, *27*, 7274−7284.
(51) Ko, H.-W.; Lee, H.-H.; Huo, L.; Xia, W.; Yang, C.-C.; Hsu, J. L.; Li, L.-Y.; Lai, C.-C.; Chan, L.-C.; Cheng, C.-C.; Labaff, A. M.; Liao, H.-W.; Lim, S.-O.; Li, C.-W.; Wei, Y.; Nie, L.; Yamaguchi, H.; Hung, M.-C. GSK3β inactivation promotes the oncogenic functions of EZH2 and enhances methylation of H3K27 in human breast cancers. *Oncotarget* **2016**, *7*, 57131−57144.
(52) Chen, B.; Guan, J.; Huang, B. Imaging Specific Genomic DNA in Living Cells. *Annu. Rev. Biophys.* **2016**, *45*, 1−23.
(53) Qin, Q.; Laub, S.; Shi, Y.; Ouyang, M.; Peng, Q.; Zhang, J.; Wang, Y.; Lu, S. Fluocell for Ratiometric and High-Throughput Live-Cell Image Visualization and Quantitation. *Front. Phys.* **2019**, *7* (), DOI: 10.3389/fphy.2019.00154.
(54) Lu, S.; Seong, J.; Wang, Y.; Chang, S. C.; Eichorst, J. P.; Ouyang, M.; Li, J. Y.; Chien, S.; Wang, Y. Decipher the dynamic coordination between enzymatic activity and structural modulation at focal adhesions in living cells. *Sci. Rep.* **2015**, *4*, 5756.

https://doi.org/10.1021/acssensors.1c01670
ACS Sens. 2021, 6, 4369−4378